Journal of Naval Architecture and Marine Engineering
December, 2023
https://doi.org/10.3329/jname.v20i2.64153 http://www.banglajol.info

INVESTIGATION OF SHEAR STRESS WITH EXPERIMENTAL STUDY AND CFD SIMULATION OF FREE SURFACE FLOWS ON A ROUND SHAPED SOLID MOVING OBJECT

C. H. Aksoy and A. Kükner
[1]Istanbul Technical University, 34469 Maslak, Istanbul, Turkey,aksoyce@itu.edu.tr
[2]Istanbul Technical University, 34469 Maslak, Istanbul, Turkey,kukner@itu.edu.tr

Abstract:
This paper presents a comprehensive study based on the results of a series of experiments conducted at different flow rates using micro-thinned sensors to obtain shear stress and velocity components around solid moving objects. The object dynamically represents marine vehicles and inflating boats through simplifications that ignore the effect of air in the object due to the complexity of capturing the viscoelastic behavior of such vehicles in simulations. Data obtained from experiments are compared with CFD simulation results to observe the accuracy and impact of flow rate on different weights. The simulation uses the Reynolds-averaged Navier–Stokes formulation with the VOF method and the turbulence models SST k-ω. Three-dimensional transient simulations are performed using the overset grid technique to define the motion of the solid object in the flow field. Uncertainty analysis was carried out for both experiments and CFD simulations. The obtained shear stress and velocity results in the simulations are valid and acceptable for different flow rates on various weights. It is also concluded and demonstrated that weight has a specific impact on the shear stress and motion of the object.

Keywords: marine vehicles, naval architecture, experimental study, glue-on sensor, hot-wire anemometer, CTA, shear stress, CFD, overset grid, VOF, SST k-ω

NOMENCLATURE

u_{ave}	average velocity
u_{max}	maximum velocity
D	hydraulic diameter
Re	Reynolds Number
f	friction factor
u^*	Friction velocity
B	additive constant
W	error rate
U	mean flow velocity
P_0	atmospheric pressure
k	turbulent kinetic energy
y	initial cell height
U_I	iterative uncertainties
U_G	grid structure uncertainties

Greek symbols

ε	Roughness
τ_w	shear stress
ρ	Density
Ƙ	von-Karman constant
θ	alignment angle of the probe
v	kinematic viscosity
v_T	turbulent viscosity
ω	turbulent dissipation rate
δ_I	iterative errors
δ_G	grid structure errors

1. Introduction

The primary objective underlying these investigations is the application of computational fluid dynamics (CFD) analysis to assess alterations in the trajectory of objects subjected to forces within free surface flows. In addition, these investigations demonstrate the precision of the results obtained through such analyses. Velocity and shear stress magnitudes were monitored via sensor instrumentation to assess the outcomes of the CFD simulations. In this context,

1813-8535 (Print), 2070-8998 (Online) Received on: Jan., 2023

the findings are deemed satisfactory. The use of CFD analysis in engineering problem solving represents a prevalent and effective approach, particularly when juxtaposed with protracted experimental endeavors that entail substantial time and financial resources. Consequently, CFD emerges as a highly viable option for addressing the aforementioned issues.

Moreover, within various domains, such as the entertainment sector, the influence of liquid flow warrants consideration. This factor significantly affects the optimization, design, and categorization of boats and vehicles, rendering accurate boat trajectory calculations pivotal in averting potential accidents and injuries stemming from computational inaccuracies. Thus, it is imperative to derive realistic results from CFD simulations, circumventing the necessity for repetitive experimentation. In this context, the calculation of velocity and shear stress components at the solid body surface within free surface flow is of critical importance. Notably, while numerous studies have investigated ship resistance, maneuverability, and hydrodynamics concerning boats and marine vehicles, both with and without propulsion systems, this study distinguishes itself in several aspects, including methodology, experimental setup, data acquisition, and results.

Given the convergence of experimental observations involving hot film sensors and CFD simulations within free surface flows, it is advisable to organize previous research endeavors into two distinct subcategories. The first category comprises studies focusing on shear stress measurement using hot-film sensors. It is essential to elucidate the technical complexities intrinsic to the experimental process, underscoring the significance of such studies. Hot-film sensors are susceptible to electrical noise during measurement, necessitating meticulous calibration and adherence to stringent measurement protocols. The delicate micro-thickness of the sensors renders their precise attachment to surfaces a challenging task. Furthermore, the accurate specification and integration of resistance values into the cables, which exhibit low resistance and are employed in sensor, jumper, and CTA interconnections, directly influence the results.
A comprehensive evaluation and scrutiny of previous studies of shear stress measurement via hot-film sensors reveals that the data acquired through these sensors are generally accurate and acceptable. Noteworthy studies include Sumer et al. (1993), who developed hot-film probes to measure bottom shear stress around a vertical cylinder, and Zhang et al. (1997), who employed shear stress measurements to determine boundary layer transition. Similarly, Sarma and Moes (2005) investigated skin friction measurements using similar sensors and, similar to the present study, employed the acquired data to validate the CFD results. Descamps et al. (2008) examined the influence of bubbles in a pipe by assessing pressure drop via hot-film sensors, whereas Binns et al. (2009) measured intermittency using comparable sensors. In the subsequent decade, the number of studies employing hot-film sensors for measurements increased. Rethmel et al. (2011) developed a novel flow-separation control method and collected data using these sensors. Packard and Bons (2012) and Chabert et al. (2012) conducted similar experiments in a wind tunnel. Ansell and Bragg (2014) focused on data collection concerning airfoil reattachment, paralleling the work of Packard and Bons and Zhang et al. Liu et al. published two articles in consecutive years, both focusing on hot-film sensors and capturing shear stress using different bridge types. Braune and Koch (2020) measured shear stress for supercritical laminar airfoils, whereas Perez et al. (2022) examined the potential impact of cavities on turbulence. In summary, these studies collectively share the commonality of employing hot-film sensors in experimental measurements, similar to the present study, to yield precise shear stress measurements.

The significance of computational fluid dynamics (CFD) in studies related to free surface flows cannot be overstated. The primary objective of this investigation is to validate the CFD-derived results using hot-film sensors. Consequently, the use of CFD as a solution methodology in analogous research endeavors assumes a pivotal role.

In the realm of CFD, Yu et al. (2022) conducted a comprehensive examination of various turbulent models in the context of open channel flow, employing 2-D CFD simulations. CFD, being a potent tool, enables the derivation of realistic outcomes employing diverse computational methodologies. Matsuda and Katsui (2022) contributed to this domain by presenting a study aimed at acquiring hydrodynamic forces and wake distributions using a distinct Reynolds-averaged Navier– Stokes (RANS) model. Shaheed et al. (2022) conducted a numerical simulation of turbulent flow under free surface conditions, employing the volume of fluid (VOF) method and two different turbulent models. The investigation by Wen et al. (2022) delved into numerical inquiries concerning shear stress characteristics in open channel flow, particularly in rough beds. Jebelli et al. (2022) conducted a study centered on numerical simulations in open channels, leveraging RANS models within CFD calculations to furnish precise results that aid in mitigating circulation within the flow medium.

Polgar et al. (2022) contributed a study encompassing CFD simulations aimed at deriving results of shear stress in hydrodynamic cavitation reactors, which were further validated through experimental means. Shriya et al. (2022) investigated the validation of CFD methodologies in the context of free surface flows, with a focus on obtaining velocity distribution profiles within the flow. Sulisetyo and Alifrananda (2022) conducted a similar study, albeit with an emphasis on the assessment of ship resistance across various Froude numbers. Kamath et al. (2019) delved into the domain of free-surface turbulence damping in RANS simulations, involving the modeling of complex flows and a comparative analysis of experimental data vis-à-vis CFD results. Zhang et al. (2019) scrutinized the effects of turbulence modeling on CFD predictions by employing sedan vehicles as test subjects to monitor the resultant effects. In the study by Nguyen et al. (2017), the impact of turbulence models on CFD-derived outcomes concerning ship resistance and wake dynamics was systematically explored.

Incorporating the modeling of free surface flow, Seyedashraf and Akhtari (2017) conducted a study in a three-dimensional framework, focusing on sharply curved channel bends. Li et al. (2015) conducted a noteworthy investigation employing the overset grid technique to simulate high Mach number multi-body interaction flows within complex flow scenarios. Although the study did not capture shockwaves, the results were deemed reliable and accurate. Godderidge et al. (2008) presented a study focusing on the simulation of free surface flows through CFD methodologies, contributing to the understanding of these intricate phenomena. Bates et al. (2003) delved into the numerical simulation of three-dimensional velocity fields in Nye channels, a comprehensive channel type, offering insights applicable to the resolution of measurement issues in such channels.

Considering the corpus of research on shear stress measurement through hot-film sensors and the integration of CFD in the domain of free surface flows, it is evident that such investigations bear substantial significance within various engineering applications. In this context, this study has significant potential to make meaningful contributions across multiple fields.

1.1 Experimental Setup

To conduct experiments related to free surface flow, a dedicated experimental setup has been meticulously designed, considering the specific requirements of the research problem. This custom-designed setup comprises an inlet for water entry, an outlet on the opposite end for water exit, and left and right sides configured to facilitate the drainage of water from the system. A shaft has been incorporated into the setup, which serves the dual purpose of securing the solid object at the desired film thickness and allowing for adjustments to enable free movement. The three dimensional model of the experimental setup is depicted in Figure 1.

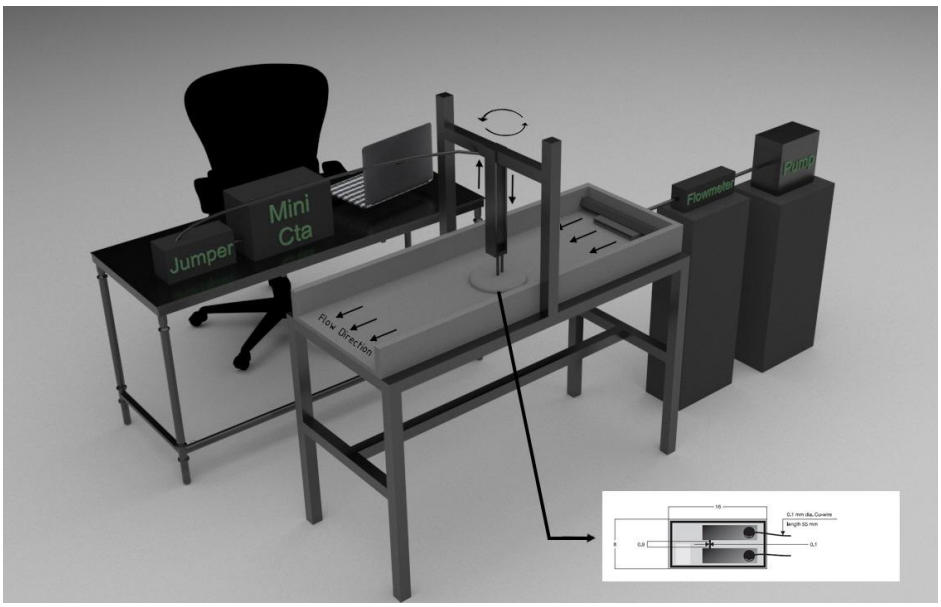

Figure 1: 3-D representation of experimental setup

Because of the unique characteristics of free surface flow, the approach to velocity measurement necessitated a multi-step procedure. Initially, the water velocity was measured at the inlet pipe using a frequency converter pump. Subsequently, after the water had spread, the velocity of the water was further measured using hot probe sensors at several locations to gather pertinent data concerning the flow profile. Specifically, a hot-probe sensor was affixed to the bottom center of the solid body to determine the magnitude of the shear stress.

For flow velocity measurements within the pipes, ultrasonic flow meters were employed. The use of these flow meters served the dual purpose of measuring flow velocity and corroborating the accuracy of the frequency converter pump at various stages throughout the experiments.

It is imperative to emphasize that to obtain accurate and reliable flow-related data, a comprehensive understanding of the sensors' working principles and characteristics is essential. These measurements are conducted at a laboratory scale, and the sensors themselves possess a delicate and fragile structure.

1.1.1. Sensors and the System

The selection of appropriate sensors is a crucial consideration in any experimental setup because the materials and characteristics of each sensor type can vary significantly, making them suitable for specific ambient conditions.

Thin quartz-coated sensors, for instance, are well suited for applications involving mid-to-low ripple frequencies in air environments. These sensors, which are categorized as the most robust among CTA probe types, are not repairable once damaged. Conversely, heavy quartz-coated sensors offer increased robustness compared with fiber sensors and are more suitable for applications involving water. Similarly, other sensor types are also non-repairable.

In the context of experimental planning, the selection and procurement of anemometers should be an integral part. Additionally, for experimental studies, a constant temperature anemometer (CTA) anemometer is frequently required to convert voltage data into meaningful values. It is imperative to ensure that the anemometer used in the experiments possesses the necessary attributes, including the required bandwidth, minimal noise levels, and bias, to yield stable and reliable results. In water applications, it is essential to verify that the CTA bridge can supply sufficient power to operate the probe at the expected flow rate.

The choice of the computer employed for CTA measurementsis generally not a critical factor. Most computers offer adequate speed and memory storage for most applications. However, it is advisable to confirm compatibility between the CTA controller, analog-to-digital (A/D) card driver, traverse driver, and the chosen computer. The software required to collect CTA measurements typically accompanies the sensors.

Figure 2 illustrates the different types of sensors used in the experiments, show casing their diversity and relevance to the study.

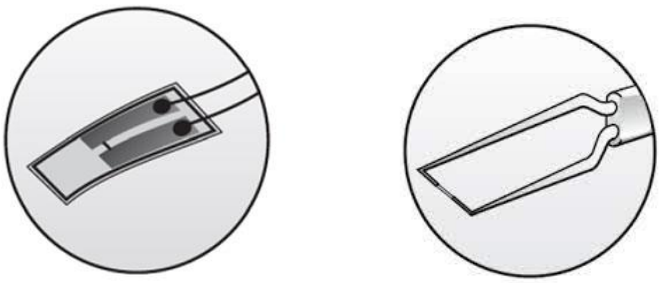

Figure 2: Hot film and hot probe sensors

The calibration system is typically not regarded as an integral component of the measurement methodology; however, it exerts a profoundly significant influence on the accuracy of the experiments to be conducted. Calibration procedures are often performed using specialized low-turbulence free jet calibrators, where velocity measurements are derived by analyzing pressure differentials at the outlet. Alternatively, if velocity values are known with clarity, they can be acquired through measurements taken within specific flow conditions. It is crucial to underscore that calibration is one of the most fundamental and indispensable aspects for achieving precise and reliable results.

Another critical consideration lies in the imperative necessity of grounding both the constant temperature anemometer (CTA) and the flow system. This grounding is deemed essential because the sensor's measurements are fundamentally based on voltage values, which are subsequently translated into the corresponding physical magnitudes. Effective grounding, therefore, forms an integral pillar in ensuring measurement integrity and minimizing the influence of external factors.

To ensure the accurate collection of data using these highly sensitive sensors, unwavering attention to the aforementioned aspects is paramount. The path followed in our experimental studies, which underscores the pivotal role of these practices in our research endeavors, is elucidated below.

1.1.2. Calibration of Instruments, Calibration Experiment and Verification

Before conducting experiments, a crucial preliminary step involved the calibration of sensors to ensure the accuracy and reliability of the collected data. To facilitate this calibration process, a dedicated calibration mechanism was meticulously designed and implemented.

The second method of calibration was chosen because of the well-established velocity values inherent to pipe flow conditions. Ensuring the accuracy of the calibration experiments necessitated the use of a filled pipe. This choice was underpinned by the fact that numerical methods, renowned for their high precision, could accurately compute velocity values under such conditions. Consequently, by introducing a controlled flow within the pipe, precise and verifiable sensor readings were attainable.

In the calibration procedure, a glue-on sensor was affixed to the end of the pipe, and systematic measurements were meticulously performed. The Mini-Constant Temperature Anemometer (Mini-CTA) device was seamlessly integrated with a computer to enable the transformation of each measurement into usable data.

To further enhance the measurement accuracy, the resistance value of each cable employed for linking the Mini-CTA devices was diligently measured and integrated into the system. Given the inherent sensitivity of the sensors used in the experiments, precise resistance measurements were conducted at the micro-level. This meticulous approach was necessitated by the susceptibility of the sensors to minute variations. These resistance values were also factored into the relevant software to ensure comprehensive calibration and data accuracy. For visual reference, the calibration experimental setup is depicted in Figure 3.

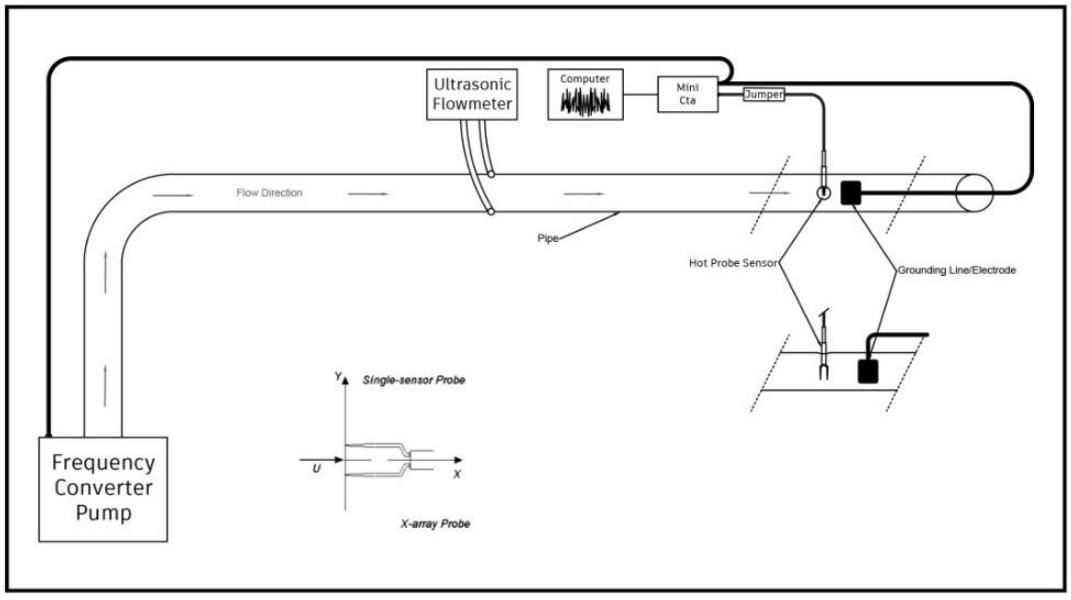

Figure 3: Calibration experiment setup

Given that the calibration process for the instruments was based on flow rate measurements, a verification test was subsequently conducted using a frequency converter pump in conjunction with an additional precision flowmeter. This meticulous verification process revealed an observed deviation of approximately 0.5% between the results. It is

important to note that the uncertainty of the flowmeter was also incorporated into the essential analysis. The verification process extended to the computational fluid dynamics (CFD) component, encompassing a comprehensive uncertainty analysis, including verification and validation procedures.

Upon examination of the calibration setup, it becomes evident that the frequency converter pump plays a pivotal role in both establishing the flow and accurately measuring the flow rate. Considering that the key input required for computational analysis is the flow rate, these devices, which have been employed in various tests and mechanisms, serve as crucial instruments for verification. The primary objective of this verification is to ensure that each instrument operates in accordance with its intended functionality and that any potential measurement errors fall within acceptable tolerances for the given application. From this perspective, the observed 0.6% deviation is deemed acceptable, particularly when considering the inherent uncertainties associated with the devices.

A critical consideration when supplying water to the relevant pipe using a frequency-adjusted pump is the potential for unnecessary turbulence and eddy formation. This phenomenon may occur as water is introduced into a pipe at a higher elevation from a lower elevation. To mitigate such measurement challenges, the pipe is adjusted to allow the flow to stabilize over a sufficient distance.

1.1.3. Jumper Settings

In addition to specifying the resistances and characteristics of all cables within the system, careful attention must be paid to the configuration of jumper settings. The establishment of these settings is crucial because they enable harmonious alignment of the interface, data transmission, and measurement components. The jumper acts as an intermediary conduit for transmitting data to the computer. Given that the jumper governs the interaction between the software and the sensor, leaving it improperly configured can lead to sensor malfunction or, in extreme cases, sensor damage. This underscores the necessity of configuring specific settings for each sensor before initiating the system.

To facilitate the configuration of jumper settings, reference tables provided by the sensor manufacturer, which delineate settings based on sensor characteristics, can be employed. A visual representation of the jumper type is depicted in Figure 4 for clarity.

Figure 4: Jumper type

1.1.4. Grounding of the Calibration Setup

Both the glue-on and hot-wire sensors used in the calibration setup, and those slated for use in subsequent experiments, are inherently susceptible to electrical interference. Consequently, precautions should be taken to shield these sensors from any form of electrification. The presence of electrification can introduce noise into the measurements and render the data inaccurate. Therefore, specific components within the setup should be grounded by establishing connections to the grounding line during the measurement processes. As previously emphasized, ensuring proper grounding for both the flow and CTA components is of paramount importance.

1.1.5. Grounding of the mini-CTA

Given that the Mini-CTA device primarily operates by interfacing with the computer, any potential electrification within this device could directly affect measurements. To safeguard against this, grounding is established by connecting a cable from the Mini-CTA's ground line to that of the frequency-regulated pump. An external cable is

affixed to the designated section on the CTA device for this purpose. This measure effectively shields the Mini-CTA from susceptibility to electrification.

1.1.6. Grounding of the Flow

Similarly, the water within the setup necessitates grounding to mitigate the risk of electrification, particularly because the sensor is situated within the flow. In this context, the ground line, which extends to the Mini-CTA, is linked to the flow using another cable. This connection ensures that the water is properly grounded.

It is imperative to note that the positioning of the grounding line in close proximity to the sensor is pivotal. Given the micro-thin dimensions of the sensors, any cable assembly may disrupt the flow current lines. Therefore, grounding is initiated from a point immediately after the sensor's termination to prevent interference with the flow's current lines.

1.1.7. Test Measurements

Within the study, measurements were conducted with the assistance of sensors post-calibration. The glue-on sensor, which is characterized as a film-type sensor suitable for precision measurements when adhered to the desired surface, is employed. Using this sensor, shear stresses beneath the solid body model are measured across various degrees of freedom. These measurements serve the purpose of comparison with the results obtained by modeling the experimental setup using computational fluid dynamics software. The primary objective of these measurements is to determine the error rate in computational fluid dynamics and to establish an analytical methodology tailored to this specific flow.

1.1.7.1. Voltage Measurements via the Hot-film Sensor

After configuring the calibration mechanism, measurements were conducted for various flow rates. The corresponding voltage values, which are correlated with these flow rates, are determined using software specifically designed for the sensors. The voltage values acquired for different flow rates via the hot-film sensor are presented in Table 1. These values are instrumental in converting voltage readings into shear stress values.

Table 1: Flow rate values and corresponding voltage values for glue-on sensor

Flow rate (m^3/ h)	**Voltage Value**
0.00	0.70
2.40	1.09
8.52	1.29
10.78	1.35
12.08	1.40
16.10	1.42
20.86	1.43
21.82	1.44

1.1.7.2 Voltage Measurements via the Hot-wire Sensor

Concurrently, measurements were performed using hot-wire sensors across a spectrum of flow rates. Subsequently, sensor-specific software was employed to determine the voltage values corresponding to these various flow rates. The voltage values derived from the hot-wire sensor for a range of flow rates are listed in Table 2. These values represent an essential dataset for the transformation of voltage data into velocity values, constituting a significant contribution to the analytical process.

Table 2: Flow rate values and corresponding voltage values for hot wire sensor

Flow rate (m^3 / h)	**Voltage Values**
1.94	5.20
3.06	5.99
4.50	5.99
6.71	7,07
8.12	7.41
9.01	7.35
13.01	8.13

1.1.8 Calculation of the Velocity Values for Calibration

The velocity values were determined during voltage measurements conducted across a range of flow rates. These measured values served as the foundation for calculating the velocity values corresponding to the respective flow rates. In addition, the magnitude of u_{max} was determined through a series of operations.

Initially, because the measured flow values were obtained from the flowmeter and were expressed in cubic meters per hour (m^3/h), these readings were divided by the cross-sectional area of the pipe and 3600, resulting in the computation of average velocity values expressed in meters per second (m/s).

The cross-sectional area of the used pipe was determined to be 0.00166 m^2. Table 3 provides a tabulation of the average velocity values along with the corresponding flow rates. The relationship between the flow rate and average velocity is presented in Table 3.

Table 3: Relationship between flow rate and average velocity

Flow Rate (m^3/h)	Average Velocity (m/s)
0.28	0.05
0.84	0.15
2.13	0.37
2,40	0.42
2.58	0.45
4.66	0.81
6.12	1.06
7.24	1.25
8.52	1.47
10.78	1.87
12.08	2.09
12.88	2.23
16.10	2.79
20.86	3.61
21.82	3.78

The calculation of average and maximum velocity values differs between laminar and turbulent flows because of their distinct nature. In laminar flows, the relationship between average velocity u_{ave} and maximum velocity u_{max} is relatively straightforward and can be expressed as follows:

$$\frac{u_{ave}}{u_{max}} = \frac{1}{2} \tag{1}$$

In equation 1, u_{ave} represents the average velocity and u_{max} is the maximum velocity. However, in turbulent flows, the relationship between these velocities is more complex because of factors such as friction factor f and relative roughness. For fully developed pipe flow in turbulent conditions, the relationship can be defined as follows:

$$\frac{u_{ave}}{u_{max}} = \left(1 + 1{,}3\sqrt{f}\right)^{-1} \tag{2}$$

To solve this equation numerically, a commonly used approach is the Colebrook equation for turbulent flows, which helps obtain the friction factor through iteration:

$$\frac{1}{\sqrt{f}} = -2\log_{10}\left(\frac{\varepsilon/D}{3{,}7} + \frac{2{,}51}{Re\sqrt{f}}\right) \tag{3}$$

where ε denotes roughness, D is hydraulic diameter, and Re is the Reynolds number. The friction factor increases with roughness. In the experiments, using pipe with smooth surface simplifies the Colebrook equation into the Prandtl equation:

$$\frac{1}{\sqrt{f}} = 2\log_{10}\left(Re\sqrt{f}\right) - 0{,}8 \tag{4}$$

Using the Prandtl equation, the friction factor can be calculated by using *f* values through an iterative process. Table 4 contains friction factors, Reynolds numbers, and velocity magnitudes obtained from these equations for specific experimental conditions.

Table 4: Calculated "f" values by iteration

Average Velocity	**Reynolds Number**	f **x10** ^{3}
0,05	2423,6	422,765
0,15	7270,8	391,745
0,37	18436,7	370,124
0,42	20773,7	367,597
0,45	22331,8	366,091
0,81	40335,7	354,421
1,06	52973,0	349,398
1,25	62667,4	346,403
1,47	73746,8	343,573
1,87	93308,7	339,602
2,09	104561,2	337,728
2,23	111485,7	336,686
2,79	139357,2	333,132
3,61	180558,4	329,143
3,78	188867,9	328,464

The primary objective is to utilize the relationship between average and maximum velocities to compute the friction velocity, which, in turn, serves as a fundamental parameter for determining shear stress. In this regard, shear stress can be expressed as follows:

$$\tau_w = \rho u^{*2} \tag{5}$$

where ρ represents density, u^* signifies friction velocity, and τ_w denotes shear stress. To acquire a shear stress value through the use of friction velocity, it is imperative to determine this parameter using the Universal Velocity Law, which is expressed as follows:

$$\frac{u_{max}}{u^*} = \frac{1}{\text{К}} ln\left(\frac{Ru^*}{v}\right) + B \tag{6}$$

Using the maximum velocity values obtained from the previous equations, friction velocity values can be determined through iterative calculations. In the equation 6, κ represents the von-Karman constant, *B* signifies an additive constant (both of which are experimentally determined), and *v* represents the kinematic viscosity, as noted by Cantwell in 2019. The von-Karman constant and the additive constant are presented as follows:

$$\text{К} = 0{,}41$$

$$B = 5$$

In this context, the shear stress values are determined by employing the specified constants and equations 5 and 6. The obtained results are presented in Table 5.

Table 5: Relationship between the flow rate and shear stress

Flow Rate (m^3/ h)	Slip Stress (Pa)
0.28	0.029
0.84	0.192
2.13	0.985
2.40	1.217
2.58	1.384
4.66	3.962
6.12	6.449
7.24	8.715
8.52	11.672
10.78	17.818
12.08	21.873
12.88	24.553
16.10	36.728
20.86	58.671
21.82	63.652

1.1.9. Voltage– Shear Stress Relationship

Given that shear stress values and voltage measurements are correlated with flow rates, it is possible to combine these two quantities and generate a graph depicting shear stresses as a function of voltage. The voltage and shear stress graph is illustrated in Figure 5.

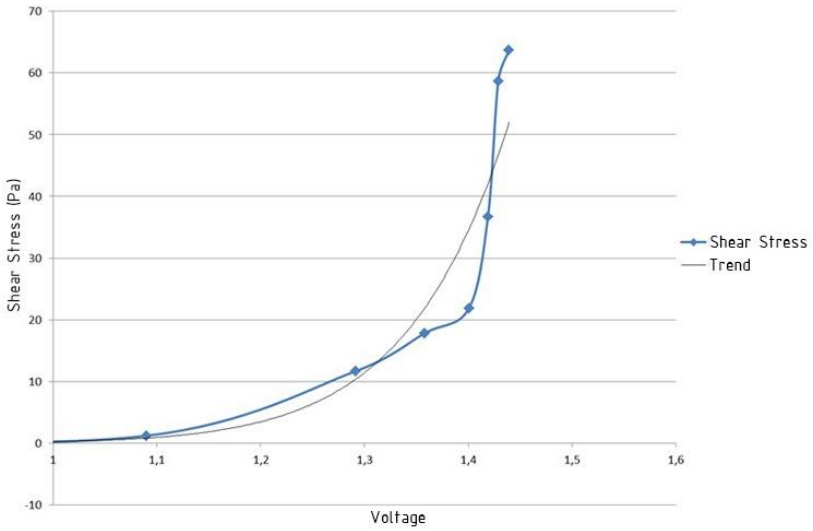

Figure 5: Voltage and shear stress relationship

1.1.10. Voltage-Velocity Relationship

The values of velocities and voltages, obtained through a hot-wire sensor and derived from flow rates, are conducive to amalgamation, culminating in the development of a graphical representation. This graph materializes as a plot of velocities against voltage, as visually illustrated in Figure 6. It provides a comprehensive visualization of the connection between velocity and the associated voltage values within the experimental context.

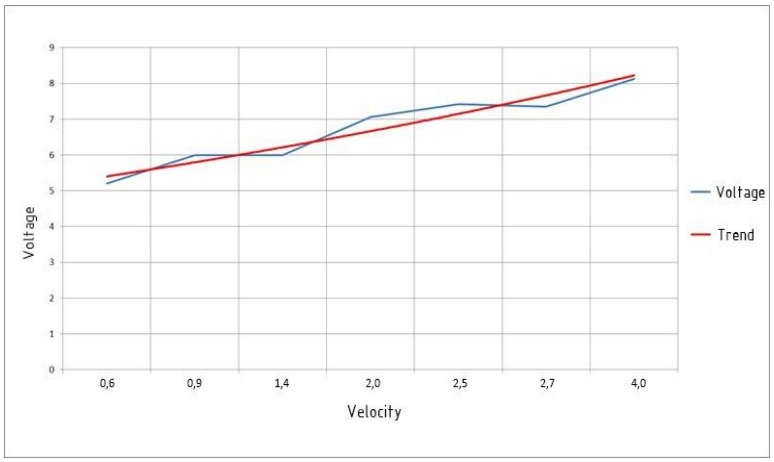

Figure 6: Voltage and velocity relationship

1.2 Uncertainty Analysis of the Experiments

While experimental studies are conducted with high-precision measuring devices, it is important to acknowledge that various errors can still arise, as is common in any experimental research. These errors and uncertainties may stem from factors such as the experimental apparatus, the system itself, device sensitivity, connection points during measurements, and the calibration of the testing equipment. Given these considerations, it becomes imperative to perform an uncertainty analysis for the conducted experimental studies.

Two widely employed methods, the ASME and ISO uncertainty analysis models, are extensively used to quantify uncertainty in experimental endeavors or analyses. Both of these methods are designed to assess the uncertainty in the results using distinct approaches while sharing a similar mathematical foundation. Consequently, the total uncertainty for the conducted study can be determined using the following formula:

$$W_R = \left[\left(\frac{\delta R}{\partial x_1} W_1\right)^2 + \left(\frac{\delta R}{\partial x_2} W_2\right)^2 + \cdots + \left(\frac{\delta R}{\partial x_n} W_n\right)^2\right]^{\frac{1}{2}} \tag{7}$$

where R is the component to be measured, n is the number of variables, and W is the error rate of the variables.

1.2.1 Uncertainty of the Ultrasonic Flow Meter

The error rate associated with the ultrasonic flow meter employed in the experiment was 1%. Ultrasonic flow meters are used in calibration studies to measure the flow rate within the pipe, a task also undertaken during the experiments. Even if the flow rate is known because of the frequency converter pump, these values are cross-verified.

1.2.2. Uncertainty of the CTA system

The uncertainty of the CTA system is contingent on the comprehensive uncertainty of the specific parameters that influence the CTA mechanism. The mechanism and experimental medium encompass numerous components that introduce potential uncertainties. All components, instruments, and medium characteristics were meticulously monitored during the experiments, and their contributions to uncertainty were determined. The total uncertainty of the CTA system can be calculated using the following formula:

$$U_{tot} = 2\sqrt{\sum u(y_i)^2} \tag{8}$$

where $u(y_i)$ is a standard deviation of the input variance.

1.2.3 Uncertainty in the Calibration Equipment

Calibration can be performed using a dedicated calibrator or alternative methodologies. Regardless of whether a calibrator is employed in the calibration process, both approaches introduce a level of uncertainty. The uncertainty associated with the calibration system or calibrator can be expressed as follows:

$$U(U_{cal}) = \frac{1}{100} SDTV(U_{calibrator}) \tag{9}$$

$$SDTV(U_{calibrator}) = a + b_{cal} \tag{10}$$

where b_{cal} and a are variables corresponding to the calibrator or system. b_{cal} may be neglected in common applications if the velocity is greater than 5 m/s. These variables are %2 and %1 as per manufacturer feedback in the experiments.

1.2.4 Uncertainty due to Linearization

Linearization is inherently related to errors stemming from curve fitting. Therefore, quantifying this value is directly associated with the errors that arise during the fitting of calibration data to the curve. The uncertainty related to linearization can be calculated as follows:

$$U(U_{lin}) = \frac{1}{100} SDTV(\Delta U_{lin}) \tag{11}$$

where $SDTV(\Delta U_{lin})$ is the standard deviation of the curve fitting errors in the calibration process in %.

1.2.5 Uncertainty of the A/D Motherboard

Because of the used devices having motherboards, the board's resolution may bring uncertainty. The mentioned value can be calculated as follows:

$$U(U_{res}) = \frac{1}{\sqrt{3}} \frac{1}{U} \frac{E_{AD}}{2^n} \frac{\partial U}{\partial E} \tag{12}$$

where E_{AD} is the *A/D* board input range, *n* is its resolution in bits, *U* is the velocity and $\frac{\partial U}{\partial E}$ is the slope of the inverse calibration curve.

1.2.6 Uncertainty due to the Position of the Probe

The impact of the probe typically introduces a minor effect into the uncertainty analysis. Although this effect is relatively small, it can be assessed using the following formula, where θ represents the alignment angle of the probe.

$$U\left(U_{pos}\right) = \frac{1}{\sqrt{3}} (1 - cos\theta) \tag{13}$$

It is a plausible approach to take into calculation this value as probe is positioned with 1°.

1.2.7 Uncertainty due to Ambient Temperature

When considering the constant temperature anemometry (CTA) system and the sensors employed in the experiments, it is imperative to consider their susceptibility to various parameters, with temperature changes being of paramount importance. Temperature fluctuations can occur between experiments, during calibration, or even within a single experiment. Hot film and hot probe sensors, in particular, are highly sensitive to temperature variations because their operation relies on heat transfer principles. These sensors utilize temperature changes to measure shear stress or velocity through micro-thin wires, subsequently converting these measurements into voltage values.

Consequently, even minor temperature changes can introduce an average error of approximately 2%. Furthermore, in the case of film sensors operating in a liquid medium, this error margin may escalate to 10%. To specify the uncertainty associated with temperature fluctuations, the following formula can be employed:

$$U\left(U_{temp}\right) = \frac{1}{\sqrt{3}} \frac{1}{U} \frac{1}{T_W - T_0} \left(\frac{A}{B} U^{0,5} + 1\right)^{0,5} \tag{14}$$

This expression provides a method for evaluating and addressing the potential influence of temperature fluctuations on the accuracy and dependability of experimental measurements, particularly for CTA sensors.

1.2.8 Uncertainty due to Ambient Pressure

Pressure variations are inherent to the heat transfer equation and define the mass flow. Probes are typically calibrated exclusively for velocity because pressure variations are considered negligible due to their minimal effects. Nevertheless, the uncertainty attributed to pressure changes can be quantified as follows:

$$U(U_P) = \frac{1}{\sqrt{3}}\left(\frac{P_0}{P_0 + \Delta P}\right) \tag{15}$$

where P_0 represents atmospheric pressure, and ΔP is the difference between the ambient reference pressure and the pressure during the measurement.

1.2.9 Uncertainty due to Ambient Humidity

In most instances, the liquid composition remains constant during calibration and experiments. Minimal variations may arise in the water vapor content (humidity) of air. This effect is exceedingly minor, typically less than 1%. Consequently, the impact of humidity on uncertainty is generally disregarded. Nevertheless, this negligible effect can be calculated as follows:

$$U(U_{hum}) = \frac{1}{\sqrt{3}}\frac{1}{U}\frac{\partial U}{\partial P_{wv}}\,\Delta P_{wv} \tag{16}$$

where $\partial U / \partial P_{wv}$ is influence on the heat transfer and ΔP_{wv} is water vapor pressure change.

1.2.10 Total Uncertainty of the CTA

Considering all components and their associated uncertainties, the uncertainty of the constant temperature anemometry (CTA) system can be estimated at 1% for typical applications, excluding calibration, in accordance with the provided formulas. However, given that calibration is an integral part of the experimental process, this uncertainty value increases to approximately 3%. The most influential variables contributing to this uncertainty are temperature and pressure changes. Therefore, it is crucial to account for the uncertainty stemming from these critical factors when conducting assessments.

1.2.11 Total Uncertainty of the Experiments

Following the calculation of CTA uncertainty using the provided equations and accounting for various external factors, the total uncertainty of the experiments was determined to be approximately 3.2%. This comprehensive assessment considers the presence of the ultrasonic flowmeter, the total CTA uncertainty, the positioning of the probe, and ambient conditions, providing a reliable estimate of the overall experimental uncertainty.

1.3. Computational Fluid Dynamics (CFD) Analysis

Shear stress measurements were conducted using a hot film sensor affixed to the underside of a solid object. Simultaneously, velocity data around the boat-like object were collected during the flow. These measurements were then compared with the values obtained from computational fluid dynamics (CFD) analysis to assess the reliability and efficiency of CFD as a solution method.

To comprehensively evaluate the flow characteristics in the CFD analysis, measurements were taken with various types of sensors with different film thicknesses. In addition, the weight of the solid body models was altered to determine its effect on the analysis. The presence of varying film thicknesses introduces lubrication effects on the surface, complicating the determination of the object's behavior in turbulent flow. Considering prior studies and literature research, the primary study parameters include the measurement of film thickness, flow rate, shear stress, and weight of the solid body, which should be carefully monitored and compared through CFD analysis.

1.3.1. Selection of Software Program for the CFD Analysis

The CFD analysis was conducted using the Cradle SC – CFD program because of its ability to deliver rapid and precise results for free surface flows. SC Flow is an advanced CFD software that employs unstructured meshes to accurately represent intricate geometries. It has been used in solving multiphase problems across diverse applications, including aerospace and automotive aerodynamics, rotating equipment such as fans and pumps, and electronic device design.

The program facilitates the generation of high-quality element meshes and the creation of intricate models. In addition, it offers seamless integration with other MSC programs such as Marc, Nastran, Adams, and Actran, enabling users to conduct multidisciplinary analyses encompassing fluid dynamics, structural mechanics, acoustics, and multi-body dynamics.

1.3.2. Selected Turbulence Model for the CFD Analysis

The turbulence model adopted for the CFD analysis is the shear stress transport (SST) *k-ω* model, chosen based on prior experiments and analysis studies that aimed to compare turbulence models in free surface flows. The SST *k-ω* turbulence model is a two-equation eddy viscosity model that has gained prominence in fluid dynamics simulations. The SST formulation combines elements of both the *k-ω* and *k-ε* models. It employs the *k-ω* formulation within the boundary layer and transitions to the k-ε model in regions away from the wall. This approach addresses the known issues associated with the *k-ω* model, making it particularly suitable for the initial stages of the study's investigations.

The governing equations of the turbulence model are defined by Menter (1994) as follows:

$$\frac{\partial k}{\partial t} + U_j \frac{\partial k}{\partial x_j} = P_k - \beta^* k\omega + \frac{\partial}{\partial x_j}\left[(v + \sigma_k v_T)\frac{\partial k}{\partial x_j}\right] \tag{17}$$

where k is the turbulent kinetic energy, U is the mean flow velocity, v is kinematic viscosity, v_T is turbulent viscosity, β and σ_k are constants.

$$\frac{\partial \omega}{\partial t} + U_j \frac{\partial \omega}{\partial x_j} = aS^2 - \beta\omega^2 + \frac{\partial}{\partial x_j}\left[(v + \sigma_\omega v_T)\frac{\partial \omega}{\partial x_j}\right] + 2(1 - F_1)_{\sigma_{\omega 2}}\ \frac{1}{\omega}\frac{\partial}{\partial x_i}\ \frac{\partial \omega}{\partial x_i} \tag{18}$$

where ω is turbulent dissipation rate, σ_ω is constant, F_1 is first pass function that can be obtained using following formula.

$$F_1 = tanh\left\{\left\{min\left[max\left(\frac{\sqrt{k}}{\beta^*\omega y}, \frac{500v}{y^2\omega}\right), \frac{4\sigma_{\omega 2}k}{CD_{k\omega}y^2}\right]\right\}^4\right\} \tag{19}$$

$CD_{k\omega}$ can be determined from the following equation.

$$CD_{k\omega} = max\left(2\rho\sigma_{\omega 2}\frac{1}{\omega}\frac{\partial k}{\partial x_i}\frac{\partial \omega}{\partial x_i}, 10^{-10}\right) \tag{20}$$

According to the model, the kinematic eddy viscosity is calculated as follows:

$$v_T = \frac{a_1 k}{max(a_1\omega, SF_2)} \tag{21}$$

The second pass function can be expressed as follows:

$$F_2 = tanh\left[\left[max\left(\frac{2\sqrt{k}}{\beta^*\omega y}, \frac{500v}{y^2\omega}\right)\right]^2\right] \tag{22}$$

The output limiting function can be obtained by using the following equation.

$$P_k = min\left(\tau_{ij}\frac{\partial U_i}{\partial x_j}, 10\beta^* k\omega\right) \tag{23}$$

1.3.3. Selected Method for the CFD Analysis

The volume of fluid (VOF) method, which is known for its effectiveness in handling two-phase flows, was employed for the analysis. The VOF method is a straightforward technique for modeling free surfaces. Essentially, a solution approach revolves around numerically identifying, tracking, and representing the free surface. The Navier– Stokes equations, which govern the flow's motion, need to be solved independently to effectively utilize the VOF method.

1.3.4. Boundary Conditions of the Geometric Model

Given the geometric symmetry of the model and the uniformity of boundary conditions on both sides, a symmetrical solution approach was adopted by considering only half of the model. This reduction in the calculation scope helps optimize computational resources. The boundary conditions used in the simulations are illustrated in Figure 7.

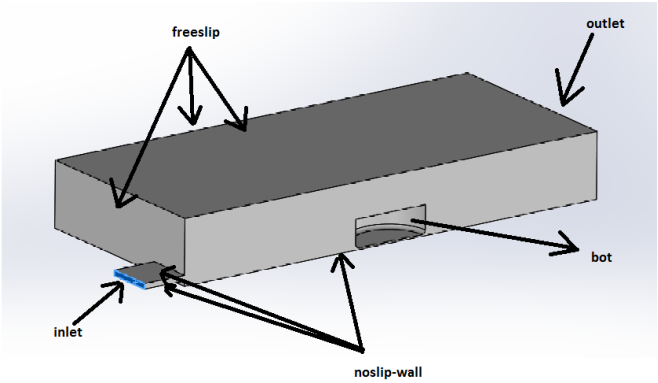

Figure 7: Boundary conditions

The slip boundary condition is defined as the parts representing the solid surface. An inlet and an outlet are formed in the geometry.

1.3.5. y^+ Value

The y^+ value is a dimensionless measure of wall distance and is of significant importance in computational fluid dynamics analysis. In essence, the y^+ value provides insights into how well the mesh used in the simulation has been constructed or modeled. It primarily indicates whether the mesh elements are sufficiently small in compared to the boundary layer thickness.

Moreover, different turbulent models require specific y^+ values, taking into account the methodology and prior research. For the SST *k-ω* model, it is crucial to maintain a y^+ value below 5 to ensure the accuracy of results obtained from the CFD analyses.

To address this consideration in the analysis, the y^+ value was adjusted to be below 5, and a mesh adaptation study was conducted to determine the y^+ value that produces realistic data from the flows.

The y^+ value can be calculated using the formula below and can also be directly observed within the computational fluid dynamics program:

$$y = \frac{y^+ \mu}{\rho u_*} \tag{24}$$

where y is the initial cell height, ρ is the density, u_* is friction velocity and μ is dynamic viscosity.

1.3.6. Time Step

The time step has been set to 0.001 s for this analysis. It is imperative to note that when calculating the y^+ value, the compatibility of the time step and mesh size should always be considered. Ensuring that these two parameters work harmoniously is essential for the accuracy and reliability of computational fluid dynamics (CFD) simulation.

1.3.7. Grid Structure

The grid structure employed in the simulations is as follows. In the experimental phase, only the flow rate was varied, whereas the same grid model was applied in the analyses conducted at different flow rates. The grid configuration used in the simulations is visually depicted in Figure 8.

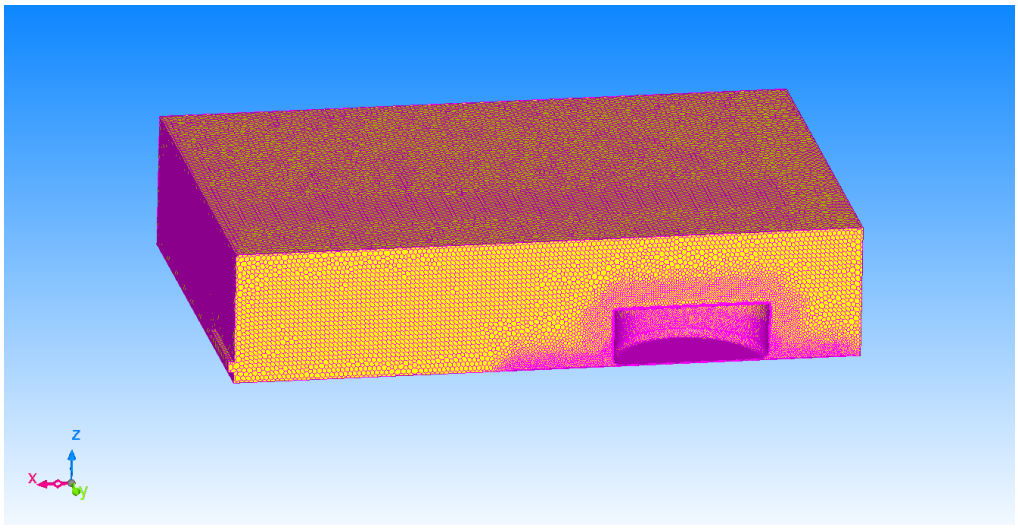

Figure 8: Grid structure

1.4. Comparison of the Experiments and Analysis

To comprehensively assess the accuracy and reliability of the experimental data and computational fluid dynamics (CFD) analysis, a series of comparisons were conducted. These comparisons encompass a range of flow rates and various liquid film thicknesses, allowing for a comprehensive evaluation of the shear stresses in the conducted experiments.

The initial set of experiments, along with their corresponding CFD analyses, focused on observing shear stresses under a constant film thickness. Subsequently, a second set of comparisons was undertaken to analyze the shear stresses acting on the free body. As an illustrative example, Figure 9 depicts the shear stress distribution at the bottom of the object, highlighting the output obtained from the simulations.

These comparative analyses serve as a critical component of the study, enabling researchers to assess the consistency and agreement between the experimental and computational results across different experimental conditions and parameter.

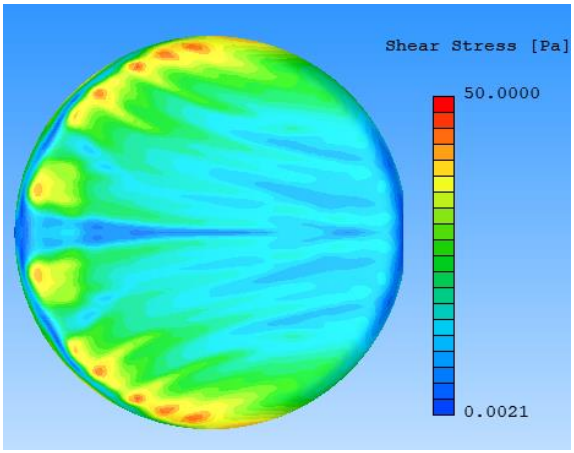

Figure 9: Shear stress distribution on the bottom

1.4.1. Comparison of the Analysis and Experiments at Constant Film Thickness

The error rates between the experimentally obtained results and the corresponding computational fluid dynamics (CFD) simulations are summarized in Table 6. These error rates were computed based on velocity measurements acquired through hot-wire sensors and their respective CFD simulations.

Table 6: Error rates (%)

Film Thickness	Nozzle Outlet Velocity (m/s)	Front (m/s)	Left (m/s)	Right (m/s)	Back (m/s)
1 mm	6.80	5.26	6.25	6.25	6.25
	6.28	5.35	5.49	5.49	5.66
	4.95	5.13	4.62	4.62	5.51
3 mm	5.73	3.23	6.98	6.98	6.67
	4.98	6.04	5.84	6.23	6.25
	5.31	4.79	5.86	5.86	6.61
5 mm	5.63	4.55	3.51	3.51	5.66
	4.32	6.34	6.72	6.72	5.26
	6.42	4.86	5.62	5.62	5.67

1.4.2. Comparison of the Analysis and Experiments at Different Weights

In parallel, a comparable methodology is employed for the examination of various weights of solid objects, and the outcomes are presented in this section. The shear stresses exerted upon objects weighing 211, 267, and 295 grams, respectively, are determined alongside the corresponding flow velocities surrounding these objects. The findings of the 211-gram object are presented in Table 7, as illustrated below.

Table 7: Experimental results

211 g – Obtained Data				
Nozzle Outlet Velocity (m/s)	Front (m/s)	Left (m/s)	Right (m/s)	Back (m/s)
5.30	1.10	1.80	1.80	0.80
6.70	2.00	2.40	2.40	1.10
Analysis Results				
Nozzle Outlet Velocity (m/s)	Front (m/s)	Left (m/s)	Right (m/s)	Back (m/s)
5.62	1.23	1.72	1.72	0.74
6.68	2.08	2.54	2.54	1.01
Error Rate %				
Nozzle Outlet Velocity	Front	Left	Right	Back
-5.69	7.56	4.65	4.65	6.67
1.36	3.85	5.51	5.51	7.84

Furthermore, in addition to the velocity measurements, the experiments also entail the measurement of the shear stress values. The shear stress results corresponding to various flow rates are presented in Table 8, as depicted below.

Table 8: Experimental results for shear stress

Shear Stress	Experiment Results (Pa)	Analysis Results (Pa)	Error Rate (%)
1 mm – Flow rate 6.9 (m^3/h)	5.32	5.04	5.48
1 mm - Flow rate 11.0 (m^3/h)	16.06	15.43	4.06
1 mm - Flow rate 15.0 (m^3/h)	27.07	28.60	5.36
3 mm – Flow rate 6.5 (m^3/h)	10.88	11.62	6.42
3 mm – Flow rate 10.6 (m^3/h)	35.39	33.45	5.79
3 mm – Flow rate 15.6 (m^3/h)	69.27	66.48	4.19
5 mm – Flow rate 7 (m^3/h)	14.90	15.86	6.07
5 mm – Flow rate 11.6 (m^3/h)	41.98	39.57	6.10
5 mm – Flow rate 16 (m^3/h)	65.80	70.91	7.21

The shear stress results for different weights are shown in Table 9.

Table 9: Experimental results for shear stress

Shear Stress	Experiment Results (Pa)	Analysis Results (Pa)	Error Rate (%)
211 g – Flow rate 6.9 (m^3/h)	4.54	4.25	6.59
211 g – Flow rate 8.6 (m^3/h)	5.00	4.70	6.53
267 g – Flow rate 9 (m^3/h)	4.73	4.98	5.05
267 g – Flow rate 16.97 (m^3/h)	6.08	6.68	8.90
295 g – Flow rate 12.5 (m^3/h)	5.44	5.09	6.84
295 g – Flow rate 18 (m^3/h)	10.93	10.08	8.41

1.5. Computational Fluid Dynamics (CFD) Uncertainty Analysis

Results acquired through computational fluid dynamics (CFD) simulations inherently encompass uncertainties and errors that contribute to deviations from precise values. Although the terms "uncertainty" and "error" are frequently used interchangeably, they possess distinct meanings upon closer examination. It is crucial to classify and assess the magnitude of these uncertainties and errors to gauge their impact on the accuracy of the results.

Mathematically, uncertainty can be defined as disparities arising from the absence of information at any stage or activity within the modeling process. Conversely, error denotes discernible disparities not stemming from a lack of information during modeling and simulation activities (Gokçe and Kınacı, 2012). In experimental studies, error is typically defined as the difference between the measured values and the true or exact values. Within this context, uncertainty serves as a means to estimate error or define the range within which the error is expected to lie.

Turbulence modeling introduces various sources of uncertainty into the CFD simulations. Given the parallels between CFD and experimental studies, it is imperative to conduct a specialized uncertainty analysis for CFD simulations to comprehensively evaluate the reliability of the results.

To conduct an uncertainty analysis, it is essential to define errors and uncertainties stemming from mathematical or geometry-based models as well as solution-based numerical and error uncertainties. The subsequent section delineates the uncertainty analysis pertinent to computational fluid dynamics analysis, as elucidated by Stern et al. (1999). The crux of this method involves computing the simulation error according to the following formula:

$$\delta_S = S - T = \delta_{SM} + \delta_{SN} \tag{25}$$

where δ_S represents the simulation error, δ_{SM} denotes modeling errors, and δ_{SN} signifies numerical errors. The simulation error is equivalent to the cumulative sum of these two error components, as evident from the equation. The computation of the simulation uncertainty is achieved through the following procedure:

$$U_S = \sqrt{U_{SN}^2 + U_{SM}^2} \tag{26}$$

where U_S represents simulation uncertainty, U_{SN} signifies numerical uncertainty, and U_{SM} denotes modeling uncertainty. Conducting the uncertainty analysis using this method necessitates the inclusion of a verification process. Verification plays a pivotal role in determining the magnitude of numerical error and uncertainties. The numerical error can be expressed as follows:

$$\delta_{SN} = \delta_I + \delta_G \tag{27}$$

where δ_I is iterative errors and δ_G is the grid structure errors. The numerical uncertainty can be obtained as follows:

$$U_{SN} = \sqrt{U_I^2 + U_G^2} \tag{28}$$

where U_I is the iterative uncertainties and U_G is the grid structure uncertainity. Iterative uncertainty can be calculated as follows:

$$U_I = \frac{1}{2}\ |S_U - S_L| \tag{29}$$

where S_U represents the maximum value of oscillation within the computational fluid dynamics simulation solution and S_L signifies the minimum value of oscillation. With the continuous advancement of technology, there has been a gradual increase in the number of mesh elements used in calculations. Consequently, the iterative uncertainty value is observed to be lower than the grid structure uncertainty value. Given this circumstance, it is plausible to perform calculations while disregarding U_G, iterative uncertainty, and error values. The computation of grid structure uncertainty is accomplished as follows:

$$U_G = \left|C_G \delta_{RE_{G1}}\right| + \left|(1 - C_G)\delta_{RE_{G1}}\right| \tag{30}$$

where C_G is a net correction factor. To calculate the net correction factor, the following formula can be used.

$$C_G = \frac{r_G^{p_G} - 1}{r_G^{p_{G_{est}}} - 1} \tag{31}$$

$p_{G_{est}}$ is a variable that depends on the mesh geometry. This coefficient changes according to the grid structure used.r_G is the Richardson extrapolation coefficient. This value can be taken as this value based on the $\sqrt{2}$ and p_G is the accuracy level of the grid structure. The accuracy level of the grid structure can be described as follows:

$$p_G = \frac{ln(\varepsilon_{32G} - \varepsilon_{21G})}{ln(r_G)} \tag{32}$$

where ε is the average result value for each mesh structure. This value can be calculated using the following equation.

$$S_M = \frac{1}{2}\ |S_U + S_L| \tag{33}$$

$\delta_{RE_{G1}}$is the error value of the first-order Richardson extrapolation approach. To obtain this value, the following formula can be used.

$$\varepsilon_{21G} = S_{M_2} - S_{M_1} \tag{34}$$

$$\delta_{RE_{G1}} = \frac{(\varepsilon_{21G})}{({r_G}^{p_G} - 1)} \tag{35}$$

In the processes of error and uncertainty analysis, two distinct approaches can be employed based on the magnitude of the grid correction factor. If this factor significantly exceeds 1, then the solution is derived in accordance with equations 34 and 35. Conversely, when the corresponding value closely approximates 1, the calculation of the corrected mesh uncertainty and corrected Richardson extrapolation error values becomes necessary, using supplementary equations. These corrected values can be acquired as follows.

$$\delta^*_{G_1} = C_G \delta_{RE_{G1}} \tag{36}$$

$$U_{G_C} = (1 - C_G)\delta_{RE_{G1}} \tag{37}$$

$$S_C = S_{M_1} - \delta^*_{G_1} \tag{38}$$

S_{M_1} is the variable depends on the simulation of the grid structure .

The validation phase encompasses the computation of the modeling uncertainty by using the experimental outcomes from the reference study. It is also plausible to identify the origins of modeling errors based on the available data. The modeling error is directly attributed to the disparity between the experimental and simulation results. Nevertheless, it should be noted that no experiment could be deemed entirely accurate when considering real-world solutions. Therefore, asserting that no modeling error can be accepted entails recognizing that verification uncertainty comprises both numerical and experimental uncertainties. The interrelation between these uncertainties is delineated as follows:

$$U_V = \sqrt{U_{SN}^2 + U_D^2} \tag{39}$$

To apply this uncertainty methodology effectively in computational fluid dynamics, it is imperative to gather a minimum of three distinct analysis results, each obtained with different mesh sizes. In this regard, three of the analyses conducted as part of the mesh adaptation study were used for the uncertainty analysis. The relationship between mesh count and shear stress is depicted in Table 10, as presented below.

Table 10: Mesh count- shear stress relationship

Mesh Count	Shear Stress Total (Pa)
350589	26.45
463291	27.79
551369	30.13
704887	30.91
1048974	30.98

The experimental uncertainty was determined to be 2.19. It is crucial to highlight that this value should surpass the uncertainty linked to the validation process; otherwise, it would suggest a systematic deviation in the results. Upon comparing the error with this value, it was established that the validation process met the pertinent criterion. Consequently, the total uncertainty is determined to be 2.19, equivalent to 6.67%.

Remarkably, the experimental uncertainty was found to be lower than the uncertainty associated with the CFD process. This observation can be attributed to the deployment of highly sensitive devices within the experimental setup and the use of a model-based RANS model in the analysis, which entails specific characteristics. Hence, it is both anticipated and acceptable to encounter this level of uncertainty in CFD simulations under these specific conditions.

1.6. Shear Stress Results

In addition to the obtained results, the calculation of the average shear stresses exerted on the body was performed. Various computations can be conducted using these average shear stress values. The results for the average shear stress corresponding to different flow rates are presented in Table 11, as depicted below

Table 11: Average shear stress results

Analysis Type	Shear Stress (Pa)
1 mm - Flow rate 6.9 (m^3/h)	7.93
1 mm - Flow rate 11.0 (m^3/h)	21.01
1 mm - Flow rate 15.0 (m^3/h)	39.38
3 mm - Flow rate 6.5 (m^3/h)	12.26
3 mm - Flow rate 10.6 (m^3/h)	33.15
3 mm - Flow rate 15.6 (m^3/h)	67.69
5 mm - Flow rate 7 (m^3/h)	16.02
5 mm - Flow rate 11.6 (m^3/h)	42.44
5 mm - Flow rate 16 (m^3/h)	75.78

The average shear stresses related to the data group that change depending on the weight are shared in Table 12.

Table 12: Shear stress results for different weights

Analysis Type	Shear Stress (Pa)
211 g – Flow rate 6.9 (m3/h)	8.25
211 g – Flow rate 8.6 (m3/h)	9.51
267 g – Flow rate 9 (m3/h)	11.28
267 g – Flow rate 16.97 (m3/h)	13.04
295 g – Flow rate 12.5 (m3/h)	11.99
295 g – Flow rate 18 (m3/h)	19.24

2. Conclusion

Experimental and numerical investigations were conducted to obtain the shear stress and velocity magnitudes acting on roundsolid surfaces. Various analyses incorporating overset grid techniques were applied to each model to obtain shear stress and velocity values. Reliable and precise flow results were obtained for the aforementioned scenarios using

these techniques. The study also includes a thorough uncertainty analysis and successfully elucidates the use of hot-film and hot-probe sensors for potential future research.

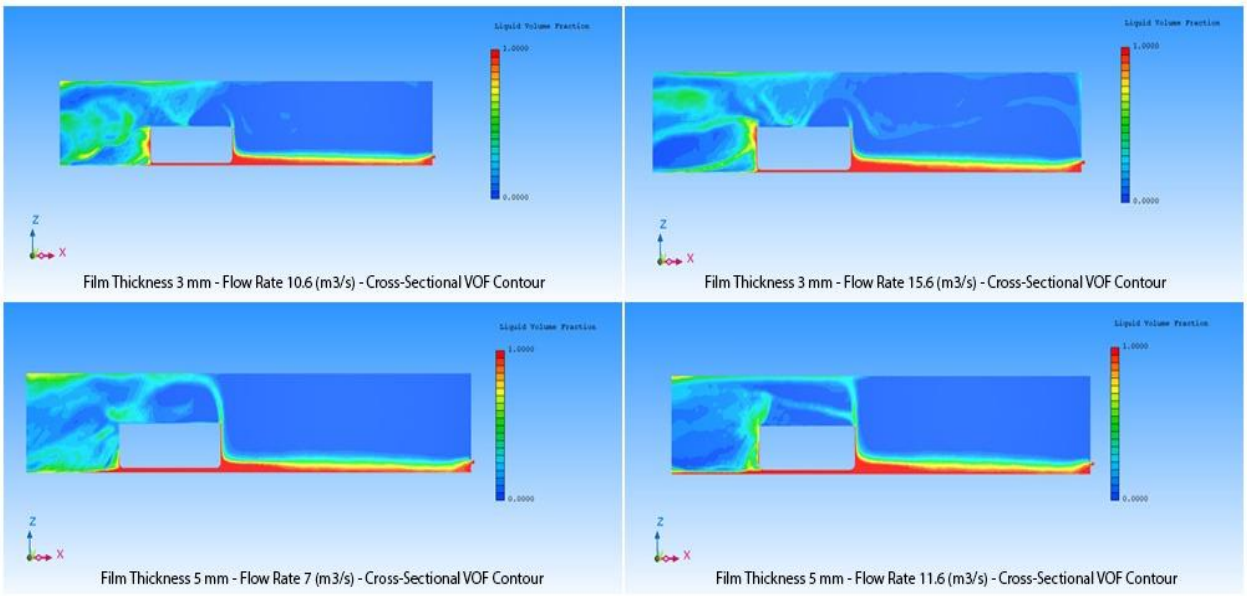

Figure 10: Cross sectional VOF contour

The cross-sectional representations of the volume of fluid (VOF) contours for multiple outcomes are visually depicted in Figures 10 and 11. These graphical illustrations reveal a notable increase in flow complexity and vorticity counts as the fluid encounters the solid mass of the buoyant object. In addition, a discernible observation can be made regarding the reduction in the thickness of the fluid film layer, particularly within the spatial domain encompassing the region between the outlet and the solid object.

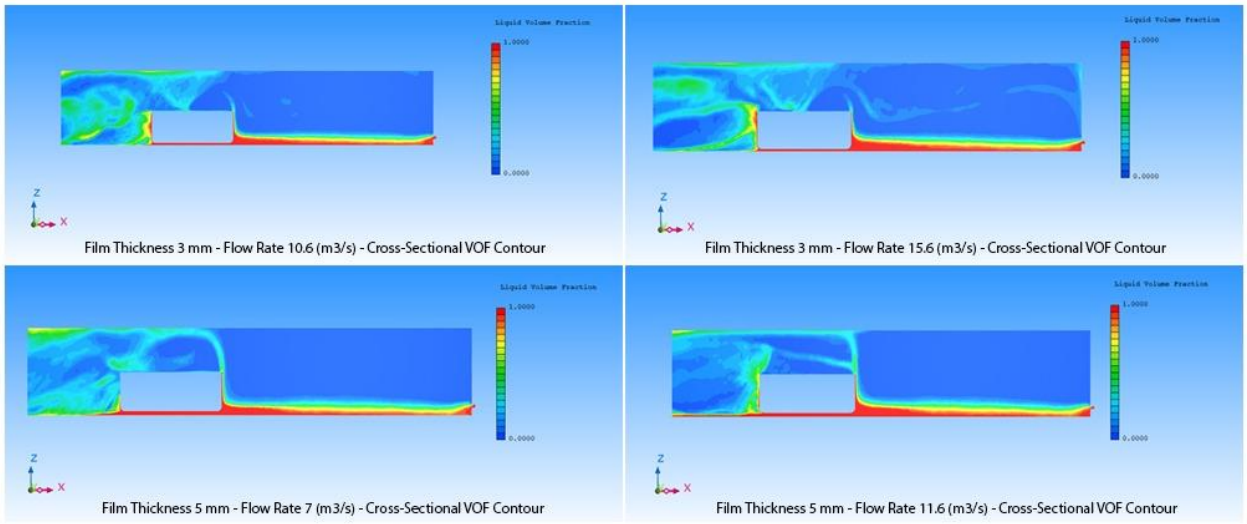

Figure 11: Cross sectional VOF contour

Figure 12 presents three-dimensional iso surfaces representing the flow field. Evidently, these isosurfaces delineate pronounced alterations in the configuration of the free surface, which result from dynamic interactions within the fluid system. Moreover, a distinct portion of the fluid attains higher elevations in response to these interactions.

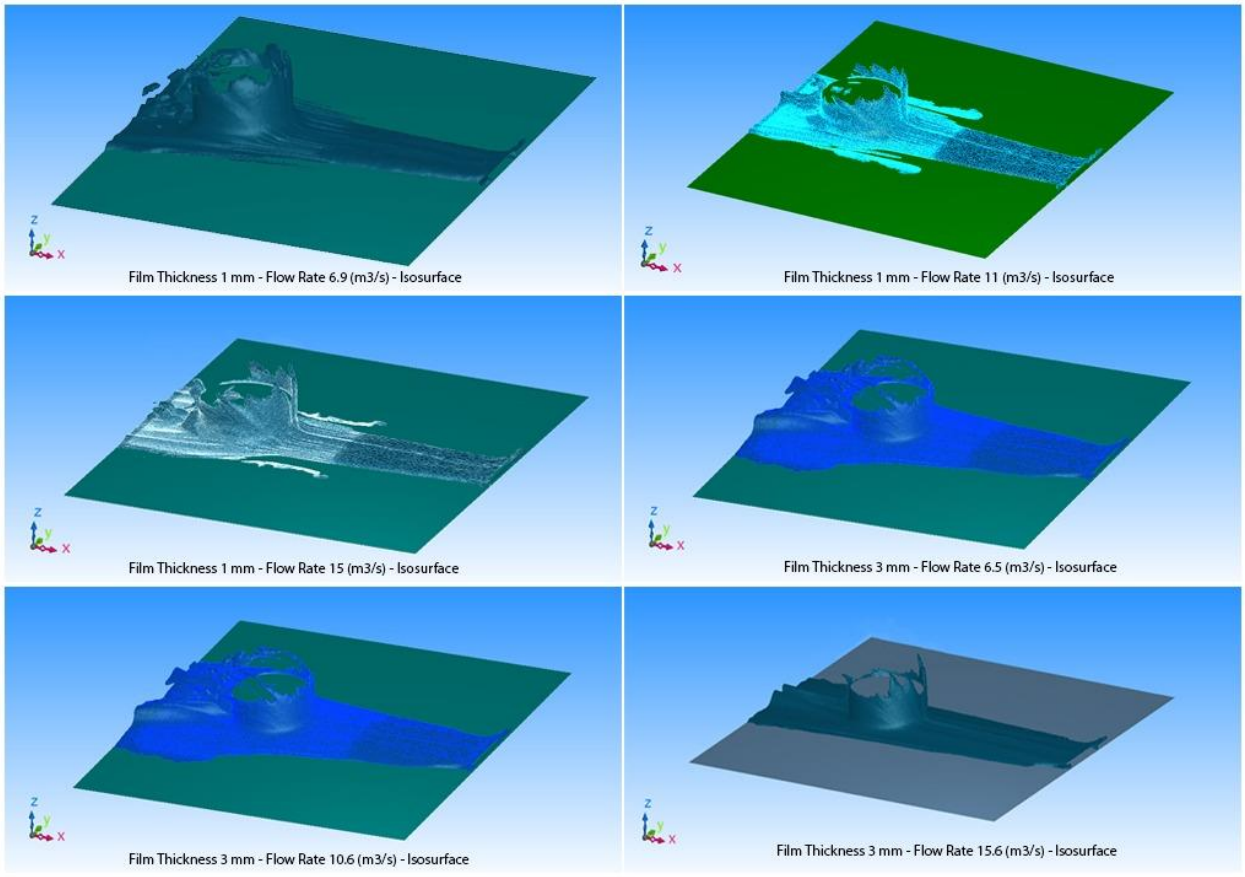

Figure 12: Isosurface

As the fluid velocity increases, there is a commensurate escalation in the forces and shear stresses exerted on the solid body's undersurface. This elevated force profile prompts the solid object to ascend to comparatively greater elevations. The formation of the film thickness becomes more conspicuous under these conditions.

The findings of this study demonstrate that accurate results can be achieved using computational fluid dynamics (CFD) tools, particularly when employing the volume of fluid (VOF) method in conjunction with the overset grid technique and using the shear-stress transport (SST) k-ω turbulent model in the SC-Flow software. Notably, the weight of the solid body was observed to have a minimal impact on both the shear stress and velocity of the solid body, whereas the flow rate exhibited a relatively higher influence on the results. In addition, the effect of thin film thickness was discernible in the results. These findings offer the possibility of designing solid surfaces to reduce bottom shear stress, thereby increasing the friction and resistance experienced by moving objects.

The primary outcome of this study underscores the accuracy of the CFD results within an acceptable range. As the initial objective of this study was to validate CFD results of shear stress, which has been successfully achieved, the potential for increasing the number of analyses to obtain further data on free surface flows is evident. Consequently, this study provides a comprehensive dataset concerning shear stress and velocity for different flow rates at various weights. The impacts of these factors on object motion were thoroughly investigated and accurately quantified through CFD simulations and experiments. Given the clear demonstration of these effects, future research may focus on the parameters highlighted here. Considering the study's results, particularly the significant influence of the object's weight on its motion and shear stress, it is advisable to consider the weight of the solid object as a primary parameter in similar research endeavors.

Acknowledgements

The authors gratefully acknowledge the financial support provided by Tübitak and Polin Group also technical support of ITUNOVA as consultant. Special thanks for Serçin BASUT, Ali CANSUN, Safa Oğuz MAZI, Sibel YILDIZ,

Onursal GÜLİSTANOĞLU, Türker İNAN, Ahmet Cihat ARIKAN and Abdulvahap KILINC. We specially thank Kadir KIRKKÖPRÜ as project consultant.

References

Ansell, P. J. and Bragg, M. B. (2014): Measurement of unsteady flow reattachment on an airfoil with an ice shape. AIAA J. 52, 656–659. https://doi.org/10.2514/1.j052519

Bates, P.D., Siegert, M. J., Lee, V., Hubbard, B. P. and Nienow, P.W. (2003): Numerical simulation of three-dimensional velocity fields in pressurized and non-pressurized Nye channels, International Glaciological Society, Annalsof Glaciology Vol:37, pp.281-285, https://doi.org/10.3189/172756403781815609

Binns, J. R. Albina, F. O. and Burns, I. A. (2009): Looking for "laminars": Measuring intermittency on the America's cup race course. Exp. Therm. Fluid Sci. 33, 865–874. https://doi.org/10.1016/j.expthermflusci.2009.03.003

Braune, M. & Koch, S. (2020): Application of hot-film anemometry to resolve the unsteady boundary layer transition of a laminar airfoil experiencing limit cycle oscillations. Experiments in Fluids volume 61. https://doi.org/10.1007/s00348-020-2907-y

Cantwell, B.J.. (2019): A universal velocity profile for smooth wall pipe flow, Journal of Fluid Mechanics, Vol. 878, pp. 834–874. https://doi.org/10.1017/jfm.2019.669

Chabert, T. Dandois, J. Garnier, E. and Jacquin, L. (2013): Experimental detection of a periodically forced turbulent boundary layer separation. Exp. Fluids 54, 1–14. https://doi.org/10.1007/s00348-012-1430-1

Cengel, Y. A., & Cimbala, J. M. (2017): Fluid mechanics: Fundamentals and applications (4th ed.). McGraw-Hill Education.

Descamps, M. N. Oliemans, R. V. A. Ooms, G. and Mudde R. F. (2008):Air-water flow in a vertical pipe: Experimental study of air bubbles in the vicinity of the wall. Exp. Fluids 45, 357–370. https://doi.org/10.1007/s00348-008-0484-6

Godderidge, B., Phillips, A.B., Lewis, S., Turnock, S.R., Hudson, D. A. and Tan, M. (2008): The simulation of free surface flows with Computational Fluid Dynamics, 2008 Ansys UK User Conference

Gokçe, M. K. and Kınacı, Ö. K. (2012): Uncertainty and error analysis for numerical solution of naval engineering problems, Yıldız Technical University

Jebelli, A.,, Mahabadi, A., Zare, M. S. and, Ahmad, R. (2022): Numerical simulations of lateral input effect in an open channel to reduce disturbances in the mainstream channel using CFD, Water-Energy Nexus Vol:5, pp:39-49, https://doi.org/10.1016/j.wen.2022.11.001

Kamath, A., Fleit, G. and Bihs, H. (2019): Investigation of Free Surface Turbulence Damping in RANS Simulations for Complex Free Surface Flows, Water 2019, 11, 456; https://doi.org/10.3390/w11030456

Li, X., Liu Y. and Qian Z. (2015): Applications of Overset Grid Technique to CFD Simulation of High Mach Number Multi-body Interaction/Separation Flow, Procedia Engineering, Vol.99, pp.458 – 476, https://doi.org/10.1016/j.proeng.2014.12.560

Liu, X. Li, Z. and Gao, N. (2018): An improved wall shear stress measurement technique using sandwiched hot-film sensors," Theor. Appl. Mech. Lett. 8, 137–141. https://doi.org/10.1016/j.taml.2018.02.010

Liu, X. Li, Z. and Gao, N. (2019): Toward calibration-free wall shear stress measurement using a dual hot-film sensor and Kelvin bridges. Meas. Sci. Technol. 29, 105303.https://doi.org/10.1088/1361-6501/aadb1b

Matsuda, S. and Katsui, T. (2022): Hydrodynamic Forces and Wake Distribution of Various Ship Shapes Calculated Using a Reynolds Stress Model, Journal of Marine Science and Engineering, Vol: 10, 777. https://doi.org/10.3390/jmse10060777

Menter, F. R. (1994): Two-equation eddy-viscosity turbulence models for engineering applications, AIAA Journal, vol. 32, no 8. pp. 1598-1605. https://doi.org/10.2514/3.12149

Nguyen, T. V., Ngo, H. V., Ibata, S. and Ikeda, Y. (2017): Effects of turbulence models on the cfd results of ship resistance and wake, Japan Society of Naval Architects and Ocean Engineers, 2017A-GS1-19

Packard N. and Bons, J. (2012): "Closed-loop separation control of unsteady flow on an airfoil at low Reynolds number. in 50th AIAA Aerospace Sciences Meeting including the New Horizons Forum and Aerospace Exposition, January American Institute of Aeronautics and Astronautics, Reston, VA. https://doi.org/10.2514/6.2012-754

Perez, A. Örlü, R., Talamelli A. and Schlatter, P. (2022): Appraisal of cavity hot-wire probes for wall-shear-stress measurements. Experiments in Fluids (2022) 63: 151. https://doi.org/10.1007/s00348-022-03498-3

Polgár, M., Agarwal, C., Gogate, P., Németh, G. and Csóka, L. (2022): Using CFD simulations to investigate the shear stress in hydrodynamic cavitation reactors coupled with experimental validation using colony count measurements, Scientifc Reports 12:18034, https://doi.org/10.1038/s41598-022-20349-7

Rathor, S. K., Mohanta, A. and Patra, K. C. (2022): Validation of computational fluid dynamics approach of lateral velocity pro curvature effect on floodplain levee of two-stage meandering channel, Research Square, DOI: https://doi.org/10.21203/rs.3.rs-1652433/v1

Rethmel, C. Little, J. Takashima, K. Sinha, A. Adamovich, I. and Samimy, M. (2011): Flow separation control using nanosecond pulse driven DBD plasma actuators. International Journal of Flow Control 3, 213–232 https://doi.org/10.1260/1756-8250.3.4.213

Sarma., G. R. and Moes, T. R. (2005): Demonstration of skin friction measurements featuring in situ estimation of conduction loss using constant voltage anemometers and surface hot-films. Rev. Sci. Instrum. 76, 055102 https://doi.org/10.1063/1.1896621

Seyedashraf, O. and Akhtari, A. A. (2017): Three-dimensional CFD study of free-surface flow in a sharply curved 30° open channel bend, Engineering Science and Technology Review, Vol: 10 (3) pp: 85-89, https://doi:10.25103/jestr.103.12

Shaheed, R., Mohammadian, A. and Yan, X. (2022): Numerical simulation of turbulent flow in bends and confluences considering free surface changes using the volume of fluid method, Water 2022, 14, 1307. https://doi.org/10.3390/w14081307

Stern, F., Wilson, R.V., Coleman, H.,W. and Paterson, E.G. (1999): Verification and validation of cfd simulations, Iowa Institute of Hydraulic Research Report, 407, https://doi.org/10.21236/ADA458015

Sulisetyono, A. and Alifrananda M. H. N. (2022): Evaluation of the ship resistance using computational fluid dynamics at various Froude numbers, ICSEDTI 2022, October 11-13, Tanjungpinang, Indonesia, https://doi.org/10.4108/eai.11-10-2022.2326428

Sumer, B. M. Arnskov, M. M. Christiansen, N. and Jørgensen, F. E. (1993): Two-component hot-film probe for measurements of wall shear stress. Exp. Fluids 15, 380–384 https://doi.org/10.1007/bf00191776

Wen, J., Chen, Y., Liu, Z. and Li, M. (2022): Numerical Study on the Shear Stress Characteristics of Open-Channel Flow over Rough Beds, Water 2022, 14, 1752. https://doi.org/10.3390/w14111752

Yu, S., Dai, H., Zhai, Y., Liu, M. and Huai, W. (2022): A comparative study on 2D CFD simulation of flow structure in an open channel with an emerged vegetation patch based on different RANS turbulence models, Water 2022, 14, 2873. https://doi.org/10.3390/w14182873

Zhang, C., Bounds, C. P., Foster, L. and Uddin, M. (2019): Turbulence modeling effects on the cfd predictions of flow over a detailed full-scale sedan vehicle, Fluids 2019, 4, 148; https://doi.org/10.3390/fluids4030148